Journal of Hydrology 595 (2021) 126012

Contents lists available at ScienceDirect

Journal of Hydrology

journal homepage: www.elsevier.com/locate/jhydrol

Research papers

Numerical study on near-field characteristics of landslide-generated impulse waves in channel reservoirs

Xiaoliang Wang [a], Chuanqi Shi [b], Qingquan Liu [a,*], Yi An [b]

[a] Department of Mechanics, School of Aerospace Engineering, Beijing Institute of Technology, Beijing 100081, China
[b] Key Laboratory for Mechanics in Fluid Solid Coupling Systems, Institute of Mechanics, Chinese Academy of Sciences, Beijing 100190, China

ARTICLE INFO

This manuscript was handled by Huaming Guo, Editor-in-Chief, with the assistance of Xiaohui Lei, Associate Editor

Keywords:
Numerical simulation
Channel reservoir
Landslide-generated impulse waves
Near field
Leading wave

ABSTRACT

Landslide-generated impulse waves (LGIWs) in channel reservoirs of mountainous regions exhibit essential differences to those in lacustrine reservoirs. We used a soil–water coupling smoothed particle hydrodynamics model to study the near-field characteristics of LGIWs in channel reservoirs. Results show that wave formation and propagation are strongly affected by the opposite bank. A three-dimensional first wave in the near field gradually transforms into a two-dimensional leading wave that travels along the channel in far field. We classify the channel reservoir into wide or narrow according to whether the first wave is visibly affected by the opposite bank. The relations between parameters of first wave and landslide parameters in the near field are obtained from a series of numerical computations. We also provide estimation formulae for the amplitude of a leading wave in a channel reservoir which is beyond the capability of former empirical relations in lacustrine reservoir. The leading wave can be used later as initial conditions for a wave propagation model. These findings are helpful for engineering estimates of LGIWs in channel reservoirs.

1. Introduction

Landslides on the banks of large reservoirs can impact quiet water and introduce high-energy waves, termed landslide-generated impulse waves (LGIWs). LGIWs pose a serious hazard to boats in the reservoir, human life and property on nearby banks, and even threaten the safety of the associated dam and downstream infrastructure. A famous LGIW, known as the Vajont giant wave, was induced by a massive landslide, destroyed several downstream villages, and caused 2000 deaths in northeastern Italy (Bosa and Petti, 2011). The impact of LGIWs can sometimes be even stronger than the landslide itself in terms of secondary hazards, especially in the reservoir. An understanding of LGIW characteristics is therefore crucial to prevent and mitigate the damage of such hazards.

The process of LGIW generation is a complicated fluid-solid coupling problem. A landslide that loses stability will first accelerate on the slope and then impact the quiet water, causing a sudden rise of water elevation with occasional rolls and sprays. The elevated water ultimately transforms into a surge after the landslide ceases. The landslide motion is a combination of translation, deformation, and even fracture, which are strongly affected by water. LGIWs therefore present a strong nonlinear fluid-solid coupling problem with high deformation of both water and landslide (Fritz et al., 2003a, 2004; Di et al., 2009). The geological and environmental conditions (e.g., topography, reservoir boundary) (Heller et al., 2009) and dynamics of the landslide itself also increase the LGIW complexity, which make the process a difficult and open scientific problem.

The leading LGIW wave is typically the biggest wave that can impact nearby infrastructure (Noda et al., 1970; Kamphuis and Bowering, 1970). The leading wave exhibits several three-dimensional (3D) characteristics that can be used to determine the subsequent surge propagation. Previous studies have therefore focused on the near-field characteristics and leading wave formation of LGIWs, rather than the entire process. Owing to the complex fluid-solid coupling and large free-surface deformation physics, theoretical progress of LGIW has been established on very simplified assumptions, which do not fully reflect the role of fluid-solid coupling on wave formation. Physical modeling has thus become an important approach to studying LGIWs. The two-dimensional (2D) behavior of LGIWs has been extensively studied with experiments by applying the landslide as a rigid body in a flume (Heinrich, 1992; Watts, 1997, 2000; Monaghan and Kos, 2000; Panizzo et al., 2002; Walder et al., 2003; Di and Paolo, 2008; Ataie-Ashtiani and

* Corresponding author.
E-mail address: liuqq@bit.edu.cn (Q. Liu).

https://doi.org/10.1016/j.jhydrol.2021.126012
Received 19 August 2020; Received in revised form 17 November 2020; Accepted 16 January 2021
Available online 28 January 2021

Shobeyri, 2008; Heller and Spinneken, 2013, 2015). Other studies performed water tank experiments to investigate the 3D properties of the leading LGIW wave by varying the shape, density, initial landslide speed, and water depth. Some useful empirical relations between the leading wave height and key physical parameters of the landslides and water depth have been obtained (Panizzo et al., 2005; Liu et al., 2005; Ataie-Ashtiani and Nik-Khah, 2008; Ataie-Ashtiani and Najafi-Jilani, 2008; Huang et al., 2009). The deformation behavior of a landslide has also been considered using granular material in 2D flume experiments (Watts, 1997; Rzadkiewicz et al., 1997; Ataie-Ashtiani and Najafi-Jilani, 2008; Fritz, 2002; Fritz et al., 2003a, 2003b, 2004; Zweifel et al., 2006, 2007; Heller and Hager, 2010; Miller et al., 2017; Mulligan and Take, 2017; Meng, 2018) and 3D water tank experiments (Mohammed and Fritz, 2010; Ren et al., 2002; McFall and Fritz, 2016) to study the impact of landslide deformation on the leading LGIW wave. These experiments have greatly enhanced our understanding of the formation and fundamental behavior of the leading LGIW wave. However, the physics of the LGIW process and especially the interaction between landslide and water are difficult to fully extract owing to measurement technique limitations of both the water wave and particularly the physical landslide process. Furthermore, it is not feasible to maintain similarity between the water flow and landslide dynamics, which makes it impossible to extend the indoor experimental results to actual large-scale LGIWs.

In addition to experimental methods, several achievements have been made in the past decade by numerically simulating LGIWs. The Lagrangian and mesh-free smoothed particle hydrodynamics (SPH) can better handle high free-surface deformation and fluid-solid interaction than mesh-based methods, and provides an efficient platform for high surface deformation of water waves, landslides, and LGIWs (Monaghan and Kos, 2000; Du et al., 2006; Schwaiger and Higman, 2007; Bui et al., 2008, 2014; Capone, 2009; Vacondio et al., 2013; Wang et al., 2016; Heller et al., 2016; Shi et al., 2016; An et al., 2016). Qiu et al. (2017) developed an SPH model to simulate the generation and transport of the LGIW surge by treating the landslide as a rigid body. Shi et al. (2016) established a fully coupled 3D fluid-solid SPH model by considering an elasto-plastic constitutive law for the landslide and a fluid-solid interface coupling technique to simulate the formation and propagation of the LGIW surge where solid deformation plays an important role.

The above experiments and numerical simulations of LGIWs have increased our understanding of the surge formation and propagation of LGIWs. However, most of these studies have been based in a simple reservoir or flume without considering topography and boundary effects on LGIW surge formation and propagation. Reservoirs in mountainous regions are usually built on narrow and deep rivers, which we term channel reservoirs in this study. There are a lot of LGIWs in channel reservoirs already happened such as Huangtian LGIW (Chen, 2011) near Xiaowan hydropower station, Tangjiaxi LGIW in Zhexi reservoir et al. (Huang et al., 2019). LGIW surge formation and propagation are greatly limited within a narrow channel and strongly affected by the opposite bank. This type of LGIW differs substantially from LGIWs in a wide lake, which we term a lacustrine reservoir, where the influences of topography and boundary on the leading wave formation can be neglected. LGIWs in channel reservoirs may exhibit different wave structures in their surge formation and propagation. This study is therefore devoted to the near-field characteristics and surge formation of LGIWs in channel reservoirs using numerical methods.

2. Numerical model

2.1. Soil-Water coupling SPH method

LGIWs represent a typical soil–water coupled process, which involves landslide motion and wave generation. To simulate this fluid-solid coupling system, we have established a novel coupled SPH model for both the landslide and water wave (Shi et al., 2016; Shi, 2018).

We discretized the governing equation of water flow using the SPH method as follows:

$$\frac{d\rho_i}{dt} = \sum_j m_j (\boldsymbol{v}_i - \boldsymbol{v}_j)\cdot\nabla_i W_{ij}$$

$$\frac{d\boldsymbol{v}_i}{dt} = -\sum_j m_j \left(\frac{P_j}{\rho_j^2} + \frac{P_i}{\rho_i^2} + \prod_{ij}\right)\nabla_i W_{ij} + \boldsymbol{g}$$

where $\boldsymbol{v}$ is particle velocity, ρ and m are density and mass for each particle, respectively, P is pressure, $\boldsymbol{g}$ is gravity, $\prod$ is an artificial viscous dissipation term to suppress spurious oscillations, subscripts i and j denote particles i and j, and W_{ij} is the kernel function, which in this study is represented by a cubic spline function (Liu and Liu, 2003):

$$W(r_{ij}, h') = \alpha_D \begin{cases} 1 - \frac{3}{2}q^2 + \frac{3}{4}q^3 & 0 \leqslant q \leqslant 1 \\ \frac{1}{4}(2-q)^3 & 1 \leqslant q \leqslant 2 \\ 0 & q \geqslant 2 \end{cases}$$

where r_{ij} is distance between particles i and j, h' is the smoothed length, $q = r_{ij}/h'$, and $\alpha_D = 1/(\pi h^3)$

$\prod_{ij}$ is shown in Eq. (4) (Monaghan, 2005):

$$\prod_{ij} = \begin{cases} -\frac{\alpha' c'_{ij}\mu_{ij}}{\rho_{ij}} & \boldsymbol{v}_{ij}\cdot\boldsymbol{r}_{ij} < 0 \\ 0 & \boldsymbol{v}_{ij}\cdot\boldsymbol{r}_{ij} \geqslant 0 \end{cases}$$

where $\mu_{ij} = h\boldsymbol{v}_{ij}\cdot\boldsymbol{r}_{ij}/(r_{ij}^2 + \eta^2)$, $\boldsymbol{r}_{ij} = \boldsymbol{r}_i - \boldsymbol{r}_j$, $\boldsymbol{v}_{ij} = \boldsymbol{v}_i - \boldsymbol{v}_j$, c' is sound speed, $c'_{ij} = \left(c'_i + c'_j\right)/2$, $\rho_{ij} = (\rho_i + \rho_j)/2$, and $\eta^2 = 0.01h^2$. The coefficient α' artificial viscous term is set as 0.01.

To maintain simplicity in the SPH method, we use the weak compression method to handle the continuity equation, where pressure is calculated by the artificial state equation (Monaghan, 2005):

$$P = B\left(\left(\frac{\rho}{\rho_0}\right)^{\gamma_1} - 1\right)$$

where $\gamma_1 = 7$, $B = c_0^2\rho_0/\gamma_1$, $\rho_0 = 1000$ kg/m^3, and c'_0 is the reference sound speed. To maintain the density fluctuation within 1%, c'_0 is set to 20 times of the maximum estimated fluid velocity.

The soil motion is modeled as a large deformation problem that considers the elasto-plastic behavior, which is discretized by the SPH method as:

$$\frac{D\rho_i}{Dt} = \sum_{j=1}^{N} m_j (v_i^\alpha - v_j^\alpha) \frac{\partial W_{ij}}{\partial x_i^\alpha}$$

$$\frac{Dv_i^\alpha}{Dt} = \sum_{j=1}^{N} m_j \left(\frac{\sigma_i^{\alpha\beta} + \sigma_j^{\alpha\beta}}{\rho_i \rho_j} - \Pi_{ij}\delta^{\alpha\beta} + F_{ij}^{n_1} R_{ij}^{\alpha\beta}\right) \frac{\partial W_{ij}}{\partial x_i^\beta} + g^\alpha$$

where α and β are 1, 2, and 3, x, y, and z are Cartesian coordinates, v is the velocity of the soil particles, $\sigma^{\alpha\beta}$ represents the total stress tensor, and $\delta^{\alpha\beta}$ is the Kronecker delta. When $\alpha = \beta$, $\delta^{\alpha\beta} = 1$; when $\alpha \neq \beta$, $\delta^{\alpha\beta} = 0$. $F_{ij}^n R_{ij}^{\alpha\beta}$ is the artificial stress to reduce the tension instability of the soil particles, where $n_1 = W(0,h)/W(\Delta x, h)$, and$F_{ij} = W_{ij}/W(\Delta x, h)$ is a coefficient to control the artificial stress magnitude, which is set as $n_1 = 2.55$.

The rate form of the elasto-plastic constitutive equation of the soil material is given as:

$$\frac{D\sigma_i^{\alpha\beta}}{Dt} = \sigma_i^{\alpha\gamma}\dot{\omega}^{\beta\gamma} + \sigma_i^{\gamma\beta}\dot{\omega}_i^{\alpha\gamma} + 2G\dot{e}_i^{\alpha\beta} + K\dot{\varepsilon}_i^{\gamma\gamma}\delta_i^{\alpha\beta} - \dot{\lambda}_i\left[3\alpha_\psi K\delta^{\alpha\beta} + \frac{G}{\sqrt{J_2}}s_i^{\alpha\beta}\right]$$

where the "·" symbol denotes the time derivative, $\dot{e}^{\alpha\beta}$ is the deviatoric strain rate tensor, $s^{\alpha\beta}$ is the deviatoric stress tensor, α_ψ is a parameter that characterizes the plastic deformation related to the dilatancy angle ψ, G and K are the shear modulus and bulk modulus, respectively, which can be calculated using the Young's modulus and Poisson ratio, $\dot{\varepsilon}^{\alpha\beta}$ is the total strain rate tensor, $\dot{\omega}^{\alpha\beta}$ is the spin rate tensor, and $\dot{\lambda}$ is the plastic factor rate. The final three variables are calculated as (Shi et al., 2016):

$$\dot{\varepsilon}^{\alpha\beta} = \frac{1}{2}\left[\sum_{j=1}^{N}\frac{m_j}{\rho_j}(v_j^\alpha - v_i^\alpha)\frac{\partial W_{ij}}{\partial x_i^\beta} + \sum_{j=1}^{N}\frac{m_j}{\rho_j}(v_j^\beta - v_i^\beta)\frac{\partial W_{ij}}{\partial x_i^\alpha}\right]$$

$$\dot{\omega}^{\alpha\beta} = \frac{1}{2}\left[\sum_{j=1}^{N}\frac{m_j}{\rho_j}(v_j^\alpha - v_i^\alpha)\frac{\partial W_{ij}}{\partial x_i^\beta} - \sum_{j=1}^{N}\frac{m_j}{\rho_j}(v_j^\beta - v_i^\beta)\frac{\partial W_{ij}}{\partial x_i^\alpha}\right]$$

$$\dot{\lambda}_i = \begin{cases} \dfrac{3\alpha_\varphi K\dot{\varepsilon}_i^{\gamma\gamma} + (G/\sqrt{J_2})s_i^{\alpha\beta}\dot{e}_i^{\alpha\beta}}{9\alpha_\varphi\alpha_\psi K + G} & f(I_1, J_2) = 0 \\ 0 & f(I_1, J_2) < 0 \end{cases}$$

where $f(I_1, J_2)$ is the Drucker–Prager yield function, where I_1 is the first principal invariant of the stress tensor and J_2denotes the second invariant of the deviatoric stress, and α_φ and k_c are Drucker–Prager parameters, which can be obtained from the friction angle φ and cohesion c.

The interaction duration between water flow and landslide motion in LGIWs is usually very short; thus the mixing between them is not obvious. Soil–water interaction is mainly governed by direct interactions across the interface contact. We therefore use the interface coupling technique to solve the soil–water coupling effects. We use the same computation technique for both soil and water in the SPH framework, but with an artificial stress model for the water phase and an elasto-plastic model for the soil phase. A soil–water interaction pair technique is developed to achieve interface coupling in the soil–water problem. Detailed numerical treatment is provided by Shi et al. (2016) and Shi (2018).

2.2. Numerical model setup

In southwest area of China, a lot of channel reservoirs are built across the mountainous valley river, which are prone to LGIW hazards. Historical LGIW hazards in channel reservoirs include Huangtian LGIW (Chen, 2011) near Xiaowan hydropower station, Tangjiaxi LGIW in Zhexi reservoir et al. (Huang et al., 2019) Therefore we set up an idealized numerical model to represent LGIW in a channel reservoir, as shown in Fig. 1. A symmetric channel with left and right bank slopes of 45° from the horizontal surface was established to model the channel reservoir. The hydrostatic water depth h was set to 100 m, the channel length was 20 times the hydrostatic water depth (2000 m), and the water density was $\rho_w = 1000\ \mathrm{kg/m^3}$.

A trapezoid-shaped landslide was initially set at the center of the left bank (Fig. 1) and released to generate a surge. All of the physical parameters required for the SPH model were selected from typical coarse-grained granular material (Biarez and Hicher, 1994; Zhang, 2006; Shi, 2018), as listed in Table 1.

Table 2 shows four estimated geometrical parameters in several LGIWs in different reservoirs or fjords. Huangtian LGIW in Xiaowan reservoir (Chen, 2011), Dayanta LGIW in Shuibuya reservoir (Huang et al., 2019), and Tangjiaxi LGIW in Zhexi reservoir (Huang et al., 2019) were all historical LGIW hazard events. Rongsong landslide could possibly make the largest LGIW that threatens the safety of Rumei hydropower station which is planned to be built on Lancang river (An et al., 2016). The above mentioned LGIW belongs more or less to LGIW in channel reservoirs. The Lituya LGIW in 1958 in Alaska in a fjord, however, seems to be a typical 2D LGIW (Fritz et al., 2001). Therefore, three geometric parameters characterizing the landslide (Fig. 1) including length Ls, width Ws, and thickness S, together with the channel width Wc listed in Table 3 are set to several combinations of dimensionless numbers to study the LGIW characteristics in channel reservoirs.

Using different combinations of these geometric parameters, we established a series of SPH models for LGIWs in channel reservoirs. The number of SPH particles of two typical examples with $Ls = 3.6$ and $S = 0.6$ and variable Ws and Wc is listed in Table 4.

Table 1
Soil parameters used in the simulations.

$\rho_s(kg.m^{-3})$	$c(kPa)$	$\varphi(^\circ)$	$\psi(^\circ)$	$E'(MPa)$	υ
1800	0	30	0	200	0.3

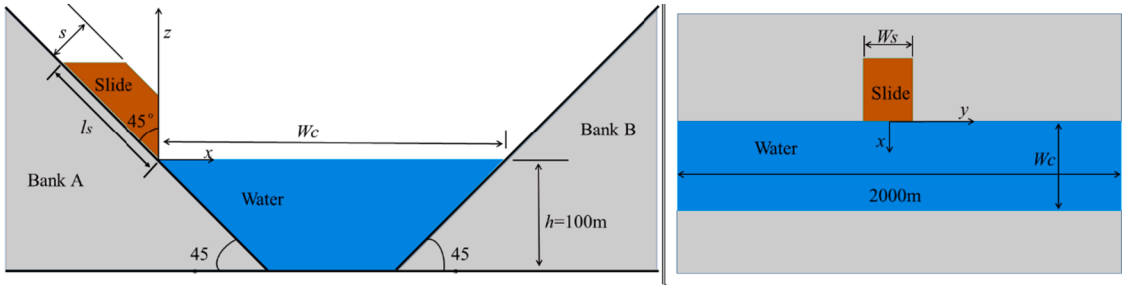

(a) Channel Profile (b) Plan view from top

Fig. 1. Schematic diagram of the wave channel and landslide.

Table 2
Key landslide and channel parameters observed in real world LGIW.

Reservoir Name	Landslide (Dimensionless) Thickness $S = s/h$	Length $Ls = l_s/h$	Width $Ws = w_s/h$	Channel Width $Wc = w_c/h$
Xiaowan	2.0	9.0	5.0	1.5 ~ 2.5
Rumei	0.4	3.5	3.0	3.0 ~ 3.9
Shuibuya	0.05	3.0	6.0	2.5
Zhexi	1.0	6.7	5.3	4.0 ~ 6.7
Lituya	0.75	8.0	6.0	11.0

Table 3
Key landslide and channel parameters in the numerical model.

Landslide (Dimensionless) Thickness $S = s/h$	Length $Ls = l_s/h$	Width $Ws = w_s/h$	Channel Width $Wc = w_c/h$
0.3 ~ 1.2, 0.6	2.4 ~ 4.8, 3.6	1 ~ 5	2 ~ 6, 2, 6

Table 4
Particle assignment in the simulations ($Ls = 3.6$, $S = 0.6$).

Condition	Boundary	Landslide	Water	TotalParticles
$Ws = 2$, $Wc = 2$	244,784	32,103	170,660	447,547
$Ws = 5$, $Wc = 6$	388,464	79,083	809,060	1,276,607

3. Results and discussions

3.1. Generation and characteristics of LGIWs

Fig. 2a–2f show the velocity fields of a typical LGIW with dimensionless parameters $Ls = 3.6$, $S = 0.6$, $Ws = 2.5$, and $Wc = 4$. After release, the landslide accelerates, rapidly deforms, and rushes into the quiet water, which results in a surge that then propagates toward the opposite bank, upstream, and downstream of the channel. Three phases are noted during the entire process. In stage 1, an elliptical surge is generated after the landslide rapidly rushes into the water and propagates in all directions, as shown in Fig. 2b and 2c. In stage 2, after the landslide has stopped, the surge runs up against the opposite bank and then falls back and forth because of gravity (Fig. 2d and 2e). In stage 3, the falling water runs both upstream and downstream along the channel with a wave front nearly perpendicular to the channel (Fig. 2e and 2f). This clearly implies that the two banks play a constraining role that limits the water wave transport in all directions but propagates along the channel direction after several up and down runs in the near-field region, which differs substantially from LGIWs in a lacustrine reservoir. For consistency, the first wave generated in the near-field by the landslide impact is called the first wave, as shown in the front of Fig. 2b and 2c. The wave traveling along the channel after leaving the near field is called a leading wave (Fig. 2e and 2f).

Fig. 3a–3d show the elevation evolution of the wave front downstream of the channel. Fig. 4 shows the wave elevation evolution along the center slice of the landslide where $y = 0$ for several positions denoted by different x-coordinates, which are made dimensionless by the water depth. The wave generated by the landslide is initially transported in all directions, then runs up and down against the opposite bank, and gradually changes transport direction to form a leading wave that travels along the channel both downstream and upstream. The bank constraint therefore strongly changes the LGIW pattern, and only part of the disturbance generated by the landslide can propagate along the channel to potentially impact infrastructure downstream and upstream.

Fig. 5 shows the wave elevation along the center of the channel ($x = Wc/2$) at several positions. The first wave initially decays quickly in the near field of the landslide; a new leading wave is then generated that propagates both upstream and downstream with a slow decay. The above phenomena imply that there is a near field where surge generation and decay are particularly important and differ between channel and lacustrine reservoirs.

3.2. Characteristics of the first wave toward the opposite bank

3.2.1. First wave generation process

The above qualitative analysis clearly demonstrates that the opposite bank plays a key role in both the generation and transport of the surge in a channel reservoir. It is therefore more appropriate to classify the channel reservoir into some typical forms that share similar surge generation and transport behavior. Fig. 6 shows the surge evolution during propagation in a wide channel ($Wc = 6$) for several landslides with different widths but constant length and thickness ($Ls = 3.6$, $S = 0.6$). For comparison, a reference case, quasi-three-dimensional (Q3D) LGIW with a width equal to the channel length ($Wc = 20$), is also shown as a red line in Fig. 6.

The results imply that the surge strongly depends on landslide width. Narrower landslides generate a weak first wave that propagates in all directions. Wider landslides generate a strong surge, even similar to the Q3D LGIW if the width is sufficient (Fig. 6). The propagation of the first wave toward the opposite bank shows several similarities, which can be divided into three regimes according to the wave amplitude.

(1) Formation regime. In this regime, the surge quickly forms owing to the interaction of the landslide with the water, and the surge elevation quickly increases until the slide stops. For narrower landslides ($Ws = 2$–4), this regime lies in region $x \leq 1$, and for wider landslides ($Ws = 6$), the formation regime lies in region $x \leq 2.5$.
(2) Decay regime. When the landslide stops, there is no energy input into the first wave. The surge decays while propagating toward the opposite bank. For narrower landslides ($Ws = 2$), the surge begins to decay at $x = 1.0$, but for wide landslides ($Ws = 6.0$), the surge starts to decay at $x = 2.5$.
(3) Edge-growth regime. In this regime, the wave elevation begins to increase owing to the growing bed near the other bank when the first wave propagates close to the opposite side. This region is approximately at the position of 1.5 times the water depth from the opposite bank.

Fig. 7 shows the water elevation evolution at four positions along the $y = 0$ section of the LGIW in channels of different widths for a landslide of $Ls = 3.6$, $Ws = 2.5$, and $S = 0.6$. The first wave generation process is the same as in a lacustrine reservoir prior to being influenced by the opposite bank; but afterward, the opposite bank strongly affects the wave propagation. For $Wc < 4$, surge formation is affected by the other bank because the channel does not supply sufficient space for surge formation. For $Wc > 4$, the three regimes clearly occur because sufficient space is provided for the landslide to run out and form the first wave. In general, $Wc = 4$ appears to be an appropriate criterion for channel reservoir-type classification according to the first wave characteristics.

We divided the channel reservoir into two channel types (wide and narrow) according to the surge formation characteristics. A wide channel is defined when $Wc \geqslant 4$. In wide channels, the opposite bank does not play a role in the formation of the first wave, the first wave exhibits full formation and decay regimes, and the surge characteristics are similar to LGIW behavior in lacustrine reservoirs.

A narrow channel is defined when $Wc < 4$. The formation of the first wave is strongly affected by the other bank because the channel does not supply sufficient space for the landslide to run out and form a surge, and the formation, decay, and edge-growth regimes overlap. In this case, the first wave characteristics are rather different than LGIWs in a lacustrine reservoir.

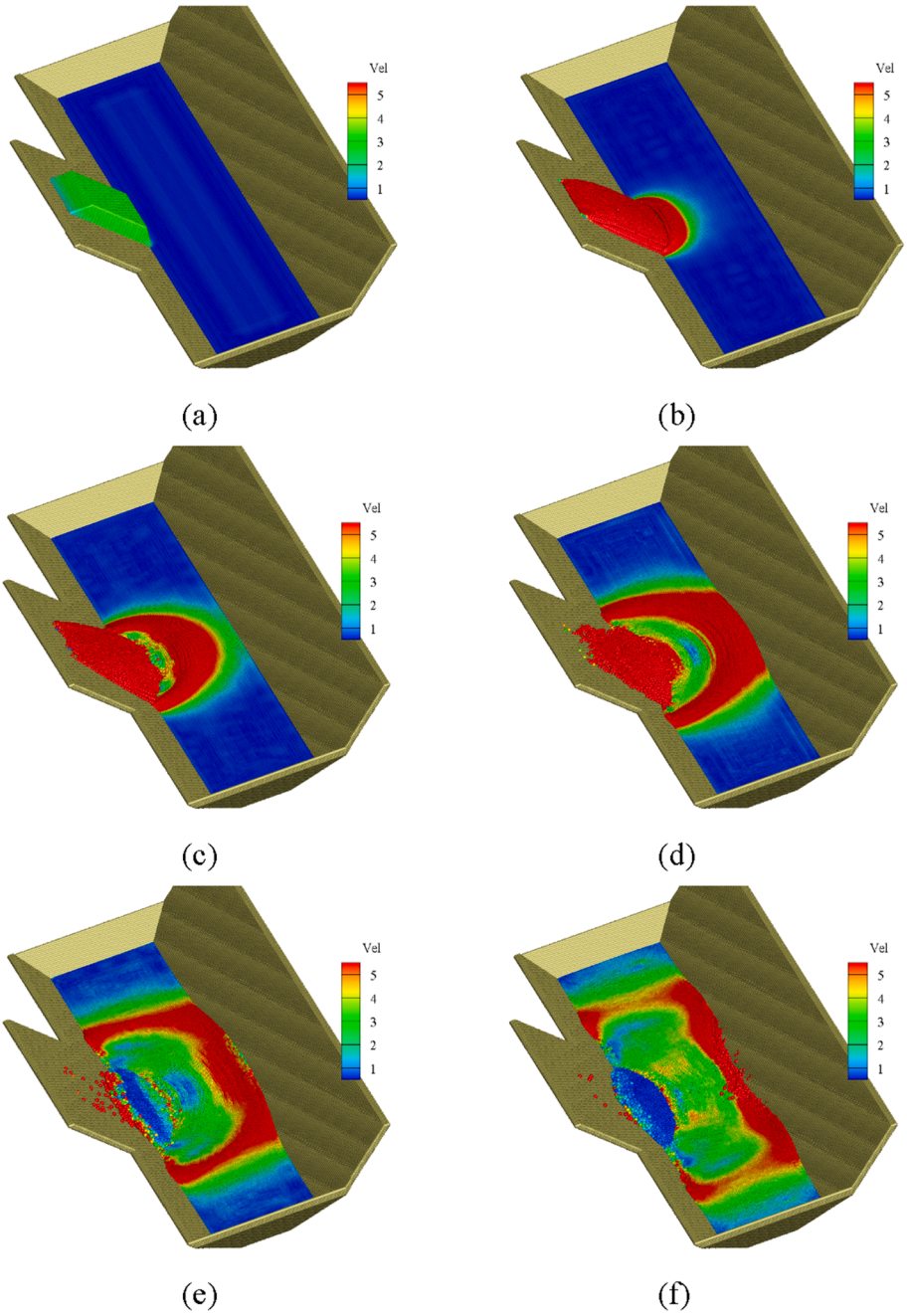

Fig. 2. Impulse wave generation process. $Ls = 3.6$, $Ws = 2.5$, $S = 0.6$, $Wc = 4$. (a) $t = 0.4$ s, (b) $t = 6$ s, (c) $t = 12$ s, (d) $t = 18$ s, (e) $t = 24$ s, (f) $t = 30$ s.

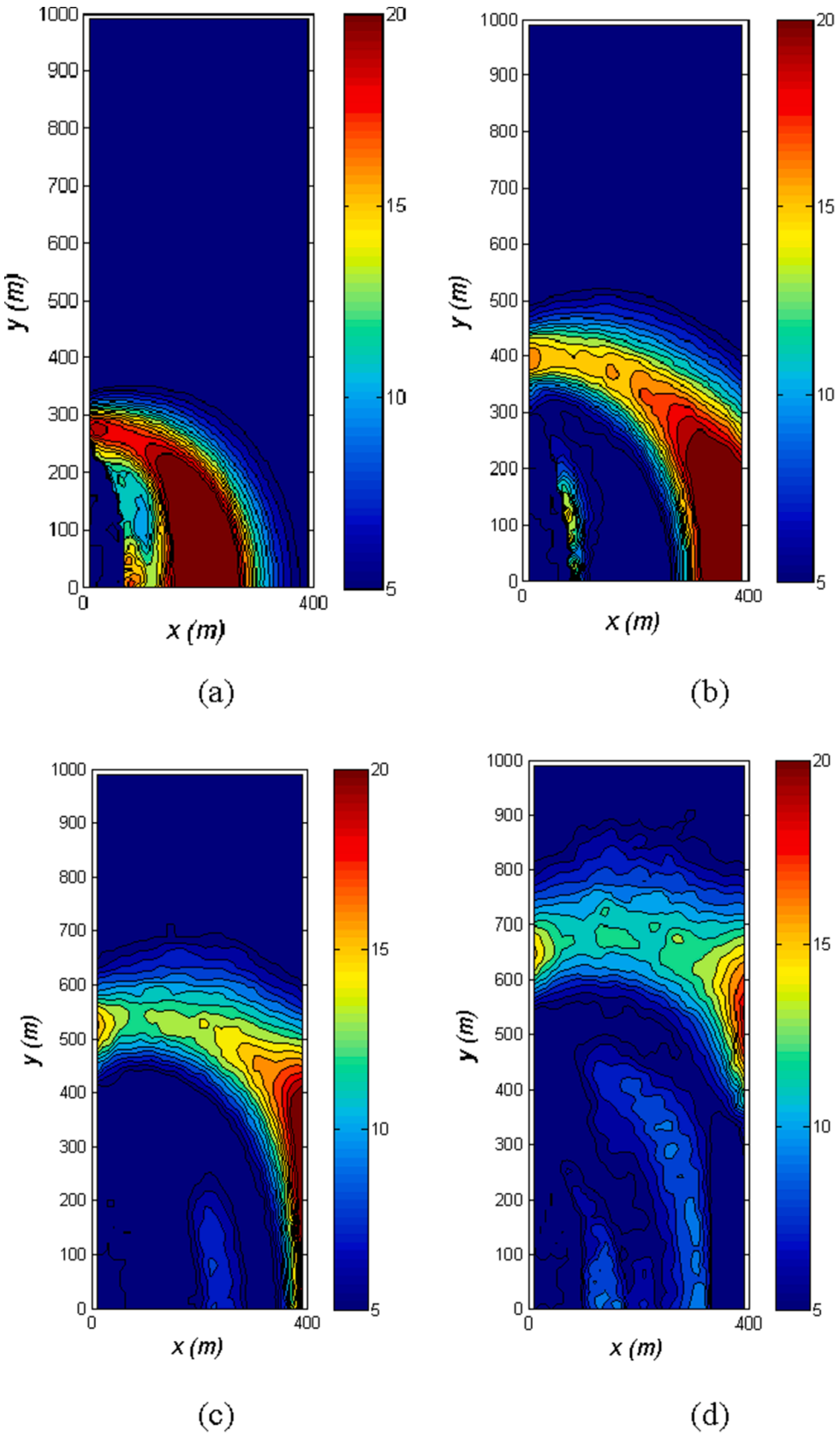

Fig. 3. Elevation of the free surface in the channel. $Ls = 3.6$, $Ws = 2.5$, $S = 0.6$, $Wc = 4$. (a) $t = 12$ s, (b) $t = 18$ s, (c) $t = 24$ s, (d) $t = 30$ s.

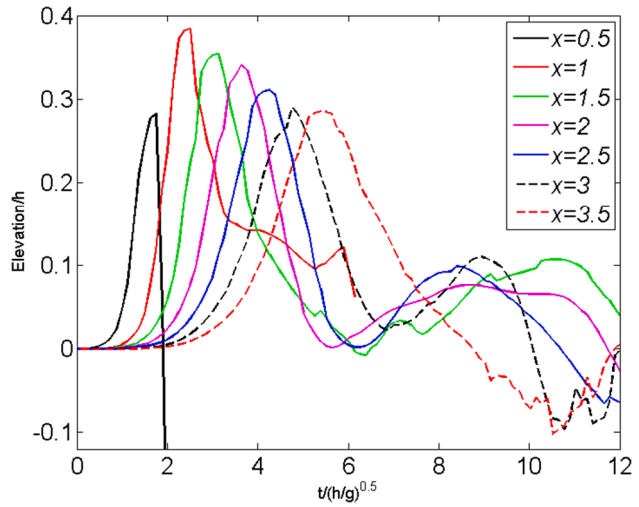

Fig. 4. Elevation of the free surface at the $y = 0$ section for several positions. $Ls = 3.6$, $Ws = 2.5$, $S = 0.6$, $Wc = 4$.

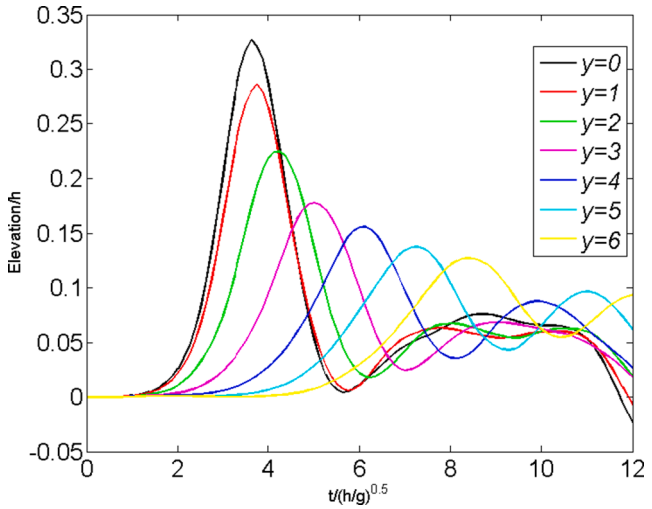

Fig. 5. Elevation of the free surface at the $x = Wc/2$ section. $Ls = 3.6$, $Ws = 2.5$, $S = 0.6$.

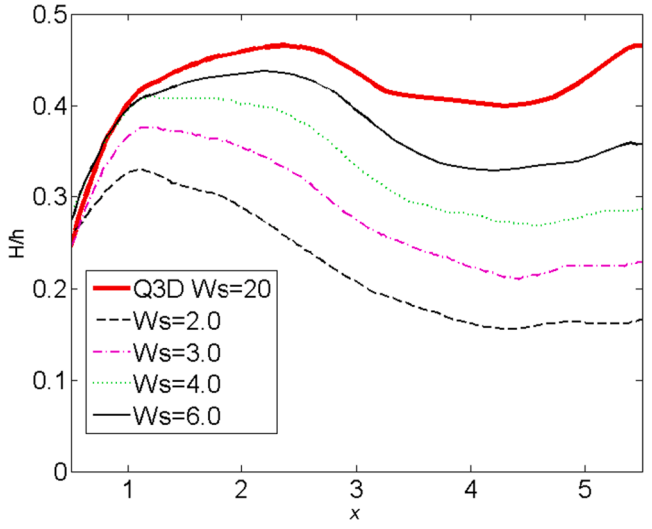

Fig. 6. Wave amplitude in the section $y = 0$. $Ls = 3.6$, $S = 0.6$, $Wc = 6$.

3.2.2. Characteristics and decay of the first wave in wide channels

The first wave in a wide channel forms after the landslide stops and begins to decay at approximately $x = 2.5$. The wave elevation at $x = 2.5$ is therefore used to characterize the first wave amplitude. For simplicity, we set $Wc = 6$, $Ls = 3.6$, and $S = 0.6$ to study the first wave characteristics in wide channels. Fig. 8 shows the wave elevations at $x = 2.5$ and 4.5 during the entire landslide process, together with the Q3D reference case. With increasing landslide width, the first wave height increases and even toward the case of a Q3D LGIW as an upper limit. However, the time when the first wave forms does not change with landslide width.

The height of the first wave depends on the landslide width in wide channels. Taking the wave height at the position where the wave starts to decay, the relationship between the dimensionless height of the first wave and landslide width is obtained by curve fitting (Fig. 9a) with a correlation coefficient of $R^2 = 0.997$ according to:

$$\frac{A_0}{A_{Q3D}} = 1 - \left(\frac{2}{3}\right)^{Ws}$$

To examine the effects of landslide length and thickness, we simulated four cases of LGIWs near the reference case where $Ls = 3.6$ and $S = 0.6$. Fig. 9b shows the results and two curves denoting 10% deviation. The height formula of the first wave in Eq. (12) is acceptable for other landslide lengths and thicknesses within a 10% deviation.

The first wave begins to decay after fully forming. A series of numerical simulations shows that the landside-generated wave is similar to a solitary wave (Fig. 8). By assuming the first wave as a solitary wave, we can therefore calculate the wave energy per unit width E_{sol} against the wave amplitude A according to solitary wave theory (Zou, 2005):

$$E_{sol} = k \cdot A^{3/2}$$

where $k = \left(8/3\sqrt{3}\right)\rho_w g h^{3/2}$. Again by assuming the first wave as a solitary wave that spreads around the wave generating point with three portions of two pieces of a quarter arc and the front of a landslide with Ws (Fig. 3a), we can obtain the total wave energy of the first wave in a channel:

$$E_C = \int_0^{\pi X + Ws} E_{sol}\ dl_C = \int_0^{\pi X + Ws} k \cdot A^{3/2}\ dl_C$$

where l_C is the length of the leading wave front.

If the first wave propagates without dissipation, we can then find the leading wave amplitude decay with transport distance:

$$\frac{A}{A_0} = \left(\frac{r + Ws/\pi}{r_0 + Ws/\pi}\right)^{-2/3}$$

where r_0 is the position where the first wave starts to decay, A_0 is the initial wave amplitude, where A denotes the amplitude of the first wave when transported to position r. In reality, the first wave dissipates energy during transport but without changing the wave pattern; thus, we may still assume that the wave amplitude during transport with dissipation shares the form of Eq. (15) but with a different exponent. We therefore use data fitting for all of the LGIW simulation cases in wide channels, yielding an equation for wave amplitude decay:

$$\frac{A}{A_0} = \left(\frac{r + Ws/\pi}{r_0 + Ws/\pi}\right)^{-1}$$

Fig. 10 compares the results of Eq. (16) with the simulation results ($R^2 = 0.93$). An exponent of -1 was also obtained by Heller and Spinneken (2015) in the first wave decay of an LGIW in a lacustrine reservoir; however, the transport distance (i.e., r in Eq. (16)) should be carefully selected in the channel reservoir because the beginning decay position r_0 differs from that in a lacustrine reservoir (Mohammed and Fritz, 2010).

To study the sensitivity of Eq. (16) to landslide shape, we consider a

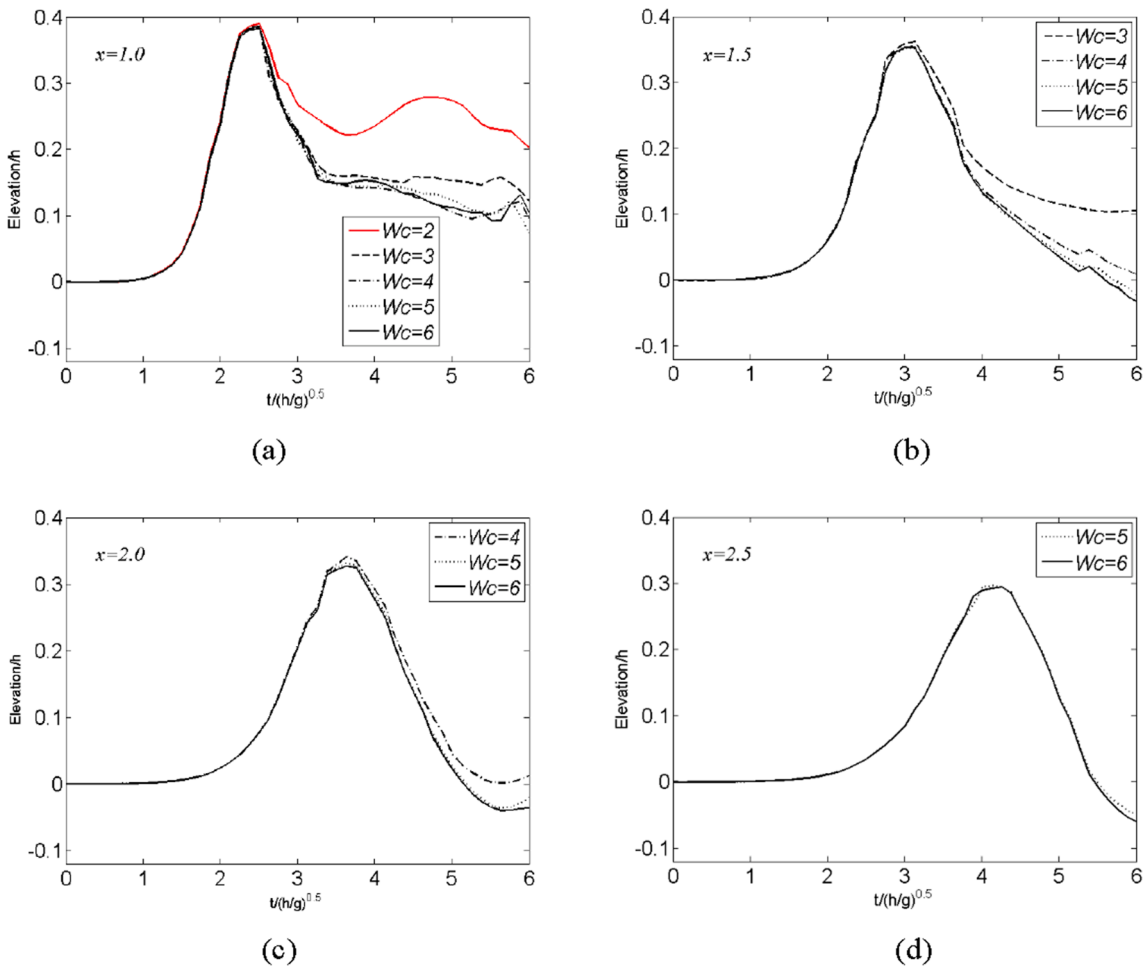

Fig. 7. Water surface elevation at the $y = 0$ section of channels with different widths. (a) $x = 1.0$, (b) $x = 1.5$, (c) $x = 2.0$, (d) $x = 2.5$.

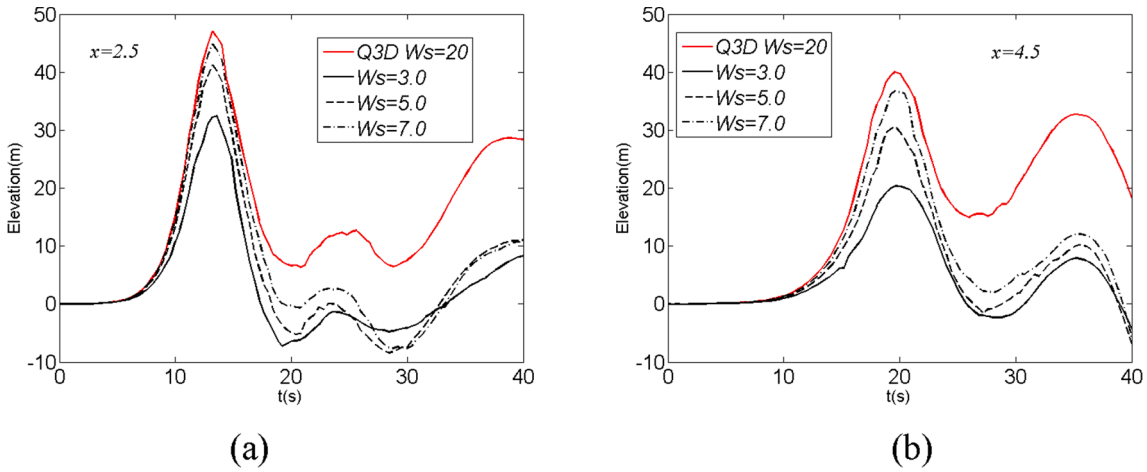

Fig. 8. Influence of landslide widths on the free-surface elevation at section $y = 0$ and (a) $x = 2.5$ and (b) $x = 4.5$. $Ls = 3.6$, $S = 0.6$, $Wc = 6$.

landslide with $Ls = 3.6$ and $S = 0.6$ as a reference and select a range of parameters Ws, Ls, and S. The simulated first wave decay behavior is shown in Fig. 11, from which we found the decay formula of Eq. (16) can still be applied within 10% deviation.

3.2.3. *Characteristics and runup of the first wave in a narrow channel*

In narrow channels, the generation and transport of a surge clearly depends on the opposite bank, which increases its analysis difficulty using conventional water wave theory. To better estimate the first wave for engineering purposes, we simulated a series of cases of LGIWs in narrow channels.

For narrow channels, we choose the height of the first wave at the center of the channel along the center line of the landslide ($x = Wc/2$, $y = 0$) to characterize its amplitude, which is made dimensionless by the leading wave height of the Q3D case. The regression analysis for the simulated cases yields the following for a first wave amplitude with Ws (Fig. 12a) together with the numerical results for $Wc = 2$ and $Wc = 3$:

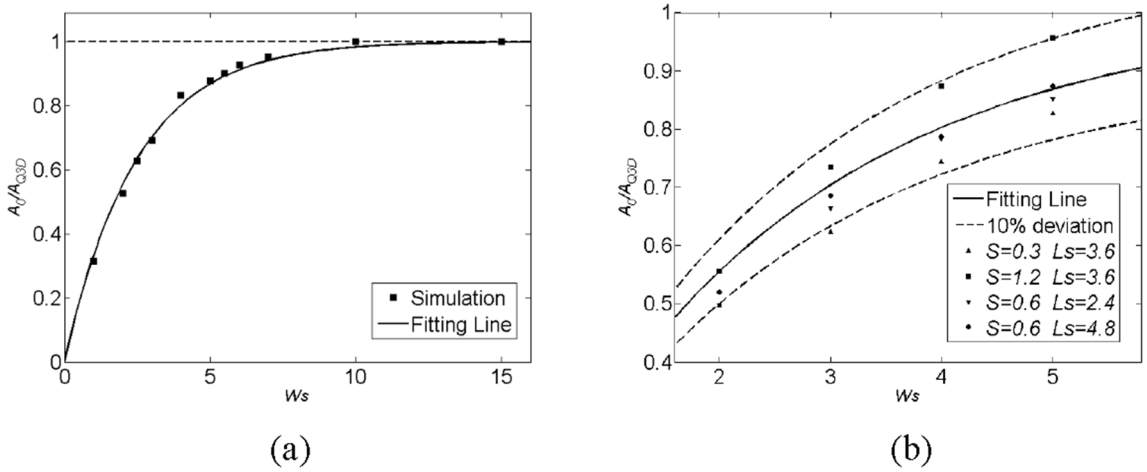

Fig. 9. (a) Comparison between simulated relative wave amplitudes and results from Eq. (12). (b) Results from Eq. (12) of cases with different *Ls* and *S* values. Dashed lines indicate ± 10% deviation.

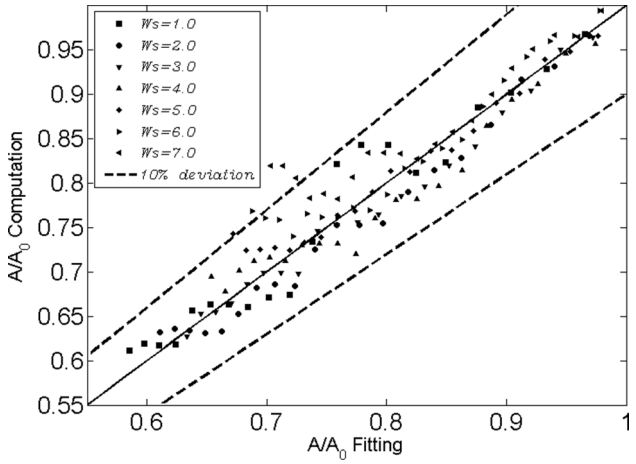

Fig. 10. Comparison between simulated relative wave amplitude and predictions using Eq. (16). Dashed lines indicate ± 10% deviation. $Ls = 3.6$, $S = 0.6$.

$$\frac{A_{narrow}}{A_{Q3D}} = 1 - 0.58^{Ws}$$

The correlation coefficient of Eq. (17) is $R^2 = 0.91$. By changing the parameters *Ls* and *S*, we simulated several cases to examine the effects of landslide shape. The results are shown in Fig. 12b. We find that Eq. (17) can be used within 25% deviation.

The runup on the opposite bank is very important for safety assessment. We therefore calculated the runups for all LGIWs in narrow channels. The regression analysis results of Eq. (18) for the runup of different landslide widths (Fig. 13a) are within 10% deviation for all of the numerical cases with a correlation coefficient of $R^2 = 0.93$.

$$\frac{R_{narrow}}{R_{Q3D}} = 1 - \left(\frac{5}{8}\right)^{Ws}$$

Some other cases were simulated to test the effects of landslide shape. The results imply that landslide shape influences the runup less than its impact on the first wave height in narrow channels (Fig. 13b), and Eq. (18) can be used within 10% deviation.

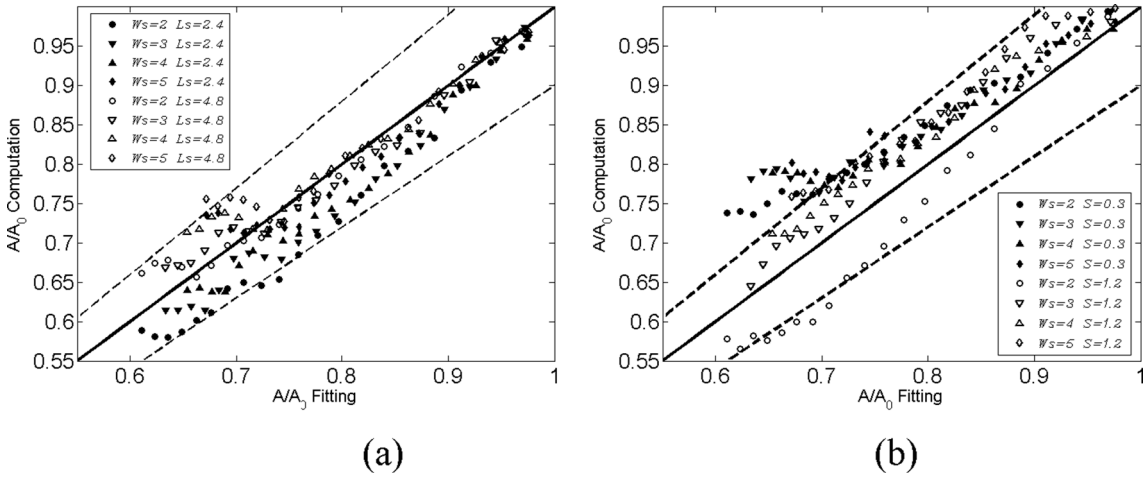

Fig. 11. Validity of Eq. (16) with different landslide parameters. Dashed lines indicate ± 10% deviation. (a) $S = 0.6$, (b) $Ls = 3.6$.

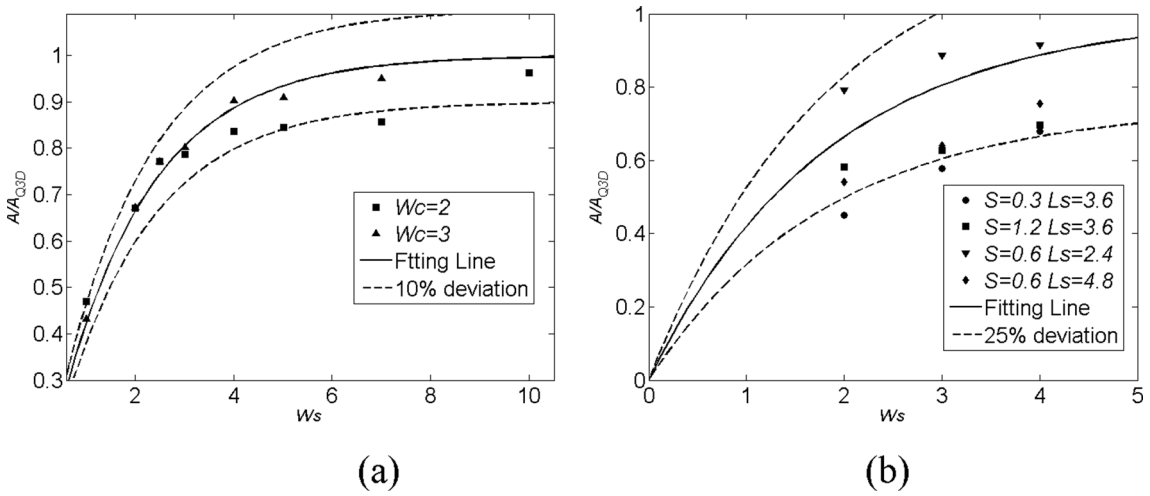

Fig. 12. (a) Comparison between simulated results of relative wave amplitude and results from Eq. (17). (b) Results from Eq. (17) applied to cases with different *Ls* and *S* values. Dashed lines indicate ± 10% deviation.

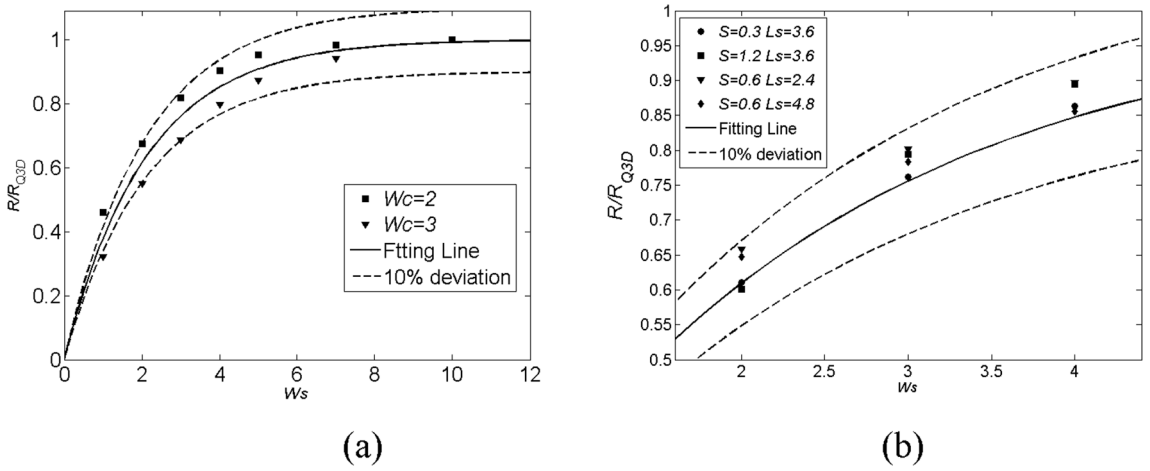

Fig. 13. (a) Comparison between simulated relative runup and results from Eq. (18). (b) Results from Eq. (18) on cases with different *Ls* and *S* values. Dashed lines indicate ± 10% deviation.

3.3. Propagation behavior of the leading wave

3.3.1. Leading wave characteristics in a channel

In many of the simulated results, we find that in a channel reservoir, the formation and transport of an LGIW clearly depend on the opposite side. In the formation phase, similar to that in a lacustrine reservoir, the water wave is generated in all directions in a circular mode owing to the impact of the landslide. When the first wave moves to the opposite bank, the wave deforms and runs up onto that bank, then returns back to the channel, and gradually changes directions and propagates along the channel. There is a transformation from a 3D near field structure into a 2D surge traveling along the channel in a channel reservoir, which differs from LGIWs in a lacustrine reservoir. The first wave in the near field of a landslide generated in a channel reservoir can therefore not be used as the leading wave that travels along the channel. The latter requires a new estimation because only the wave traveling along the channel can impact infrastructure in the channel far from the landslide occurrence.

In a channel reservoir, only the leading wave that transforms from a complex 3D near-field first wave can make an impact on the dam far away downstream. However, the transform process is quite complex. When the wave front is nearly perpendicular to the channel and the wave height is nearly constant along the wave front, this wave can be considered as the leading wave along the channel.

The widths of the landslide and channel are two factors to be considered for the transformation of the 3D first wave in near field to the 2D leading wave along the channel. In general, the transformation takes place at a farther distance with increasing landslide or channel width. The simulation results show that the transformation finishes at approximately $Y_C = Ws/2 + Wc$, where the generated 3D first wave changes into a 2D leading wave traveling along the channel. Fig. 14 shows the wave heights at different positions along $Y_C = Ws/2 + Wc$ crossing the channel for simulations with different channel and landslide widths. The wave along the crossing section at $Y_C = Ws/2 + Wc$ can be approximately considered as a leading wave that travels mostly along the channel.

In summary, a leading wave that travels along the channel approximately forms at position $Y_C = Ws/2 + Wc$. We therefore make a division for the entire channel reservoir: the near field where the surge is generated is defined as the region where $|Y| \leqslant Y_C$, and the far field where a leading wave traveling along the channel is defined as the region where $|Y| > Y_C$. In the near field, strong water-soil interactions occur in the wave generation phases, as well as complex wave motion including wave decay, runup, and gradual transformation into a 2D leading wave along the channel. In the far field, the 2D leading waves travel both upstream and downstream along the channel, which can be well simulated by the long shallow water or Boussinesq equation. In real case applications of LGIWs, we can divide the entire LGIW problem into two phases: a near-field wave generation and a far-field traveling wave.

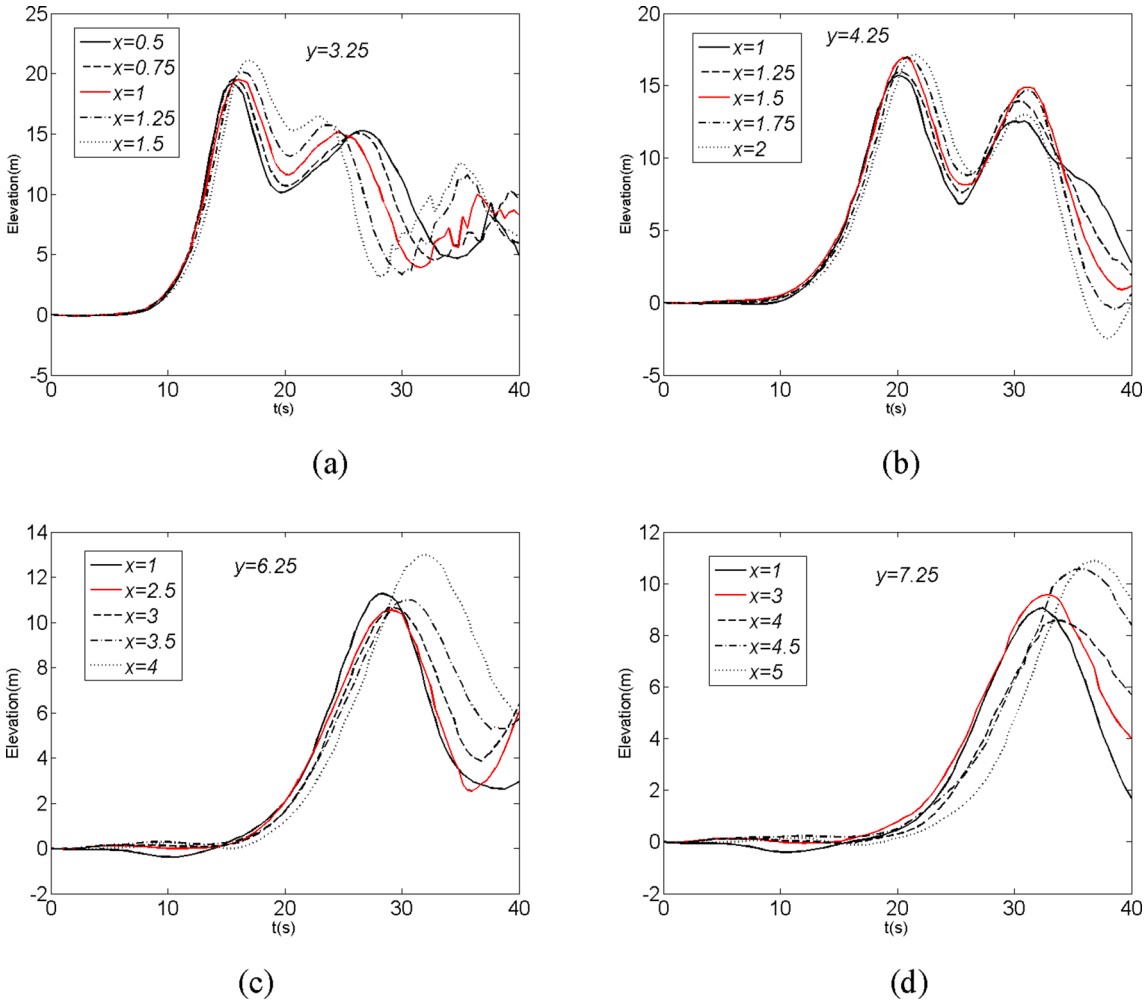

Fig. 14. Elevation of the free surface in section $Y_C = Ws/2 + Wc$ for LGIWs in channels. $Ws = 2.5$, $Ls = 3.6$, $S = 0.6$. (a) $y = 3.25$, (b) $y = 4.25$, (c) $y = 6.25$, (d) $y = 7.25$.

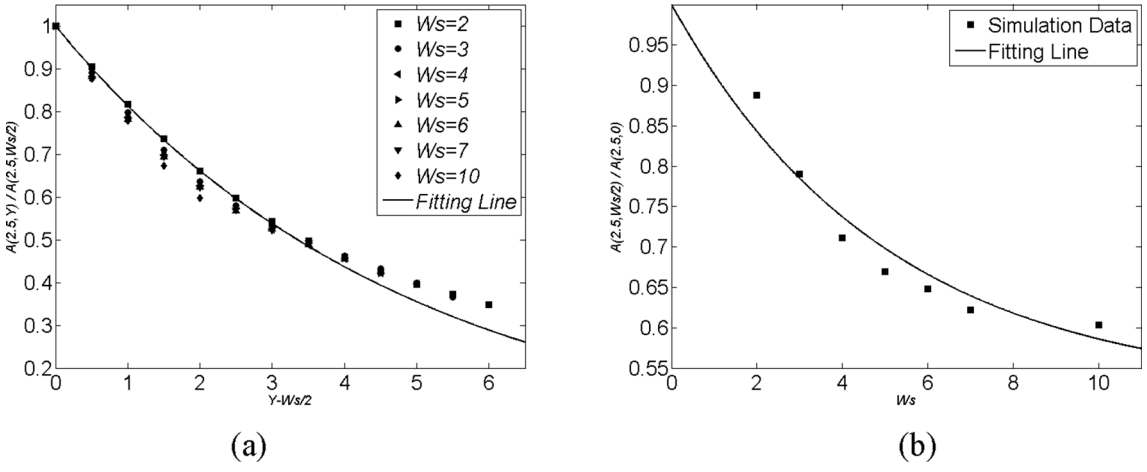

Fig. 15. Comparison between simulation results of relative wave amplitude and results from (a) Eq. (19) and (b) Eq. (20). $Ls = 3.6$, $S = 0.6$.

3.3.2. Estimation of leading wave height in wide channels

To simulate a leading wave traveling in a channel during the second phase, the initial conditions must be known. The results of the present study yield an approximate amplitude of the leading wave in the near field with variable combinations of channel width and landslide shapes for wide channels (Wc = 4–6). To more accurately analyze the leading waves, we also define a wave impact region of $|Y| \leqslant Ws/2$ where soil–water interaction plays a key role, and a wave diffusion region of $Ws/2 \leqslant |Y| \leqslant Yc$ where complex wave interaction and transformation occurs. The wave amplitude at the fringe of the wave impact region ($x = 2.5$, $y = Ws/2$), $A(2.5,\ Ws/2)$, is chosen as an approximate reference for the leading wave to travel along the channel.

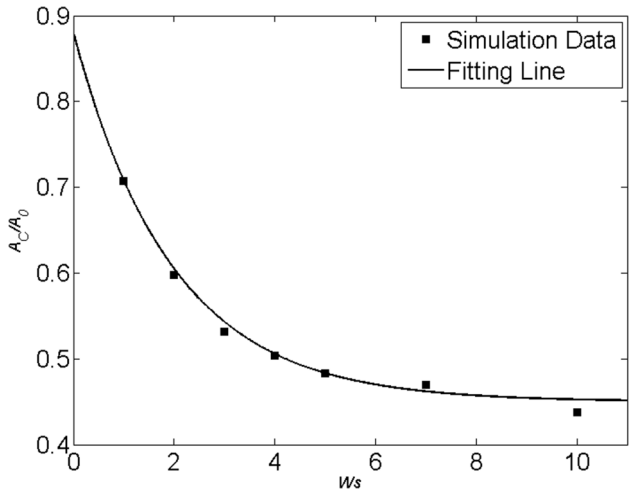

Fig. 16. Comparison between simulated results of relative wave amplitude and those from Eq. (21). $Ls = 3.6$, $S = 0.6$, $Wc = 2$.

We performed a regression analysis for the leading wave height generated by landslides of variable width and constant length and height ($Ls = 3.6$, $S = 0.6$) in a typical wide channel case with $Wc = 6$. The leading wave amplitude varies with transport distance, as shown in Fig. 15a. The fitted equation is given in Eq. (19) with a correlation coefficient of 0.98 for the leading wave along the channel, which is made dimensionless by the wave height $A(2.5,\ \ Ws/2)$ at the fringe of the impact region:

$$\frac{A(2.5,\ \ Y)}{A(2.5,\ \ Ws/2)} = 0.813^{Y-Ws/2}$$

where $A(2.5,\ \ Ws/2)$ is the wave height at position ($x = 2.5, y = Ws/2$), and $A(2.5,\ \ Y)$ denotes the wave height at position ($x = 2.5, y > Ws/2$). Fig. 15a shows that after $y = Ws/2 + Wc$, the wave amplitude slightly decays while traveling upstream or downstream.

The leading wave along a wide channel is transformed from the complex 3D wave in the near field during the surge generation phase. From the above analysis, we can approximately determine the leading wave amplitude from the surge height without considering the complex 3D transformation process. The wave amplitude at the fringe of the impact region can be obtained from its relation with the first wave amplitude in the generation phase with a correlation coefficient of 0.93:

$$\frac{A(2.5,\ \ Ws/2)}{A(2.5,\ \ 0)} = 0.52 + 0.48 \cdot 0.82^{Ws}$$

$A(2.5,\ \ 0)$

3.3.3. *Estimation of leading wave height in narrow channels*

The situation is slightly different for narrow channels. For example, the surge formation, decay, and runup stages overlap; thus there is not a clear first wave, as found in Section 5.3. We therefore directly fit the data for a leading wave along a wide channel at $Y_C = Ws/2 + Wc$ for different landslide width in a typical narrow channel ($Wc = 2$). The initial wave amplitude is made dimensionless by the wave amplitude where it begins to decay, which is approximately at $x = 1$ and $y = 0$ for LGIWs in narrow channels:

$$\frac{A_C}{A_0} = 0.45 + 0.43 \cdot 0.6^{Ws}$$

where A_C is the height of the leading wave in a narrow channel at $Y_C = Ws/2 + Wc$ and A_0 is the height of the first wave, which can be estimated by Eq. (17) for narrow channels. Eq. (21) yields a correlation coefficient of 0.99 (Fig. 16).

4. Conclusion

We studied the near-field characteristics of landslide-generated impulse waves in a channel reservoir using a newly established SPH model for soil–water interaction. The conclusions are summarized as follows.

1. In a channel reservoir, the near-field characteristics of a landslide-generated impulse wave differs from that in a lacustrine reservoir owing to the influence of the opposite bank. The generation and transport of the surge can be divided into three phases: a) a sudden rise of water owing to the landslide impact that forms a first wave in all directions; b) the surge running up on the opposite bank and returning to the channel in a back and forth manner; and c) a leading wave traveling along the channel upstream and downstream.
2. There are three regimes in the propagation of the first wave toward the opposite bank: a formation regime; a decay regime; and an edge-growth regime. Channels can be classified into either wide or narrow according to whether the first wave is strongly affected by the opposite bank. Several numerical results show that a channel with a dimensionless width (i.e., channel width over water depth) greater than four can be considered a wide channel; otherwise, it is considered a narrow channel. In wide channels, the first wave completely forms before propagating to the opposite bank and three regimes are clearly observed, which is similar to that in lake-like reservoirs. In narrow channels, the first wave's formation is strongly affected by the opposite bank and the three regimes overlap.
3. The first wave of landslide-generated water waves exhibits three-dimensional characteristics in reservoirs that largely depend on landslide width. Through regression analysis of the numerical simulations, we obtained empirical relations of the first wave amplitude in a wide channel and landslide width and wave decay behavior. For a narrow channel, the first wave amplitude and run up height were also obtained for landslides with different widths.
4. In a channel reservoir, the first wave generated by landslides will gradually transform into a leading wave traveling upstream and downstream along the channel. The numerical simulation results imply that at about $|Yc| = Ws/2 + Wc$, the leading wave along the channel forms, which can be used as an approximate initial condition for the later wave traveling in the channel by the shallow water model or Boussinesq equation. An estimation relation for the leading wave amplitude is also given for both wide and narrow channels for several landslide types.

CRediT authorship contribution statement

Xiaoliang Wang: Investigation, Data curation, Software, Visualization, Writing - review & editing. **Chuanqi Shi:** Investigation, Software. **Qingquan Liu:** Supervision, Conceptualization, Methodology, Conceptualization, Funding acquisition. **Yi An:** Data curation, Visualization, Funding acquisition.

Declaration of Competing Interest

The authors declare that they have no known competing financial interests or personal relationships that could have appeared to influence the work reported in this paper.

Acknowledgments

This study was financially supported by the National Natural Science Foundation of China (12032005, 11672310 and 11602278), National Key R&D Program of China (2018YFC1505504), and "Beijing Institute of Technology Research Fund Program for Young Scholars". We thank Esther Posner, PhD, from Liwen Bianji, Edanz Editing China (www.liwenbianji.cn/ac), for editing the English text of a draft of this manuscript.

References

An, Y., Shi, C.Q., Liu, Q.Q., 2016. Assessment of characteristics and transports of landslide generated impulse waves in reservoirs. Engineering Reports, Beijing (In Chinese).

An, Y., Wu, Q., Shi, C.Q., Liu, Q.Q., 2016. Three-dimensional smoothed-particle hydrodynamics simulation of deformation characteristics in slope failure. Geotechnique 66 (8), 670–680.

Ataie-Ashtiani, B., Najafi-Jilani, A., 2008. Laboratory investigations on impulsive waves caused by underwater landslide. Coast. Eng. 55 (12), 989–1004.

Ataie-Ashtiani, B., Nik-Khah, A., 2008. Impulsive waves caused by subaerial landslides. Environ. Fluid Mech. 8 (3), 263–280.

Ataie-Ashtiani, B., Shobeyri, G., 2008. Numerical simulation of landslide impulsive waves by incompressible smoothed particle hydrodynamics. Int. J. Numer. Meth. Fluids 56 (2), 209–232.

Biarez, J., Hicher, P.Y., 1994. Elementary Mechanics of Soil Behaviour. Balkema, Rotterdam.

Bosa, S., Petti, M., 2011. Shallow water numerical model of the wave generated by the Vajont landslide. Environ. Modell. Software 26 (4), 406–418.

Bui, H.H., Fukagawa, R., Sako, K., Ohno, S., 2008. Lagrangian meshfree particles method (SPH) for large deformation and failure flows of geomaterial using elastic-plastic soil constitutive model. Int. J. Numer. Anal. Meth. Geomech. 32 (12), 1537–1570.

Bui, H.H., Kodikara, J.K., Bouazza, A., Haque, A., 2014. A novel computational approach for large deformation and post-failure analyses of segmental retaining wall systems. Int. J. Numer. Anal. Meth. Geomech. 38 (13), 1321–1340.

Capone, T., 2009. SPH numerical modelling of impulse water waves generated by landslides. Sapienza University of Rome.

Chen, C., 2011. Destabilizing mechanism analysis and stability evaluation of a large accumulation bank slope at an alpine George reservoir. Chengdu University of Technology, Chengdu (In Chinese).

Di, Risio, M., Paolo, S., 2008. Analytical modeling of landslide-generated waves. J. Waterw. Port Coastal Ocean Eng. 134 (1), 53–60.

Di, Risio, M., Bellotti, G., Panizzo, A., De, Girolamo, P., 2009. Three-dimensional experiments on landslide generated waves at a sloping coast. Coastal Engineering 56 (5-6): 659-671.

Du, X.T., Wu, W., Gong, K., Liu, H., 2006. Two dimensional SPH simulation of water waves generated by uunderwater landslide. J. Hydrodyn. 21 (5), 579–586.

Fritz, H.M., Hager, W.H., Minor, H.E., 2001. Lituya Bay case: rockslide impact and wave run-up. Science of Tsunami Hazards 19 (1), 3–22.

Fritz, H.M., 2002. Initial phase of landslide generated impulse waves. ETH Zurich.

Fritz, H.M., Hager, W.H., Minor, H.E., 2003. Landslide generated impulse waves, Part 1: Instantaneous flow fields. Exp. Fluids 35 (6), 505–519.

Fritz, H.M., Hager, W.H., Minor, H.E., 2003. Landslide generated impulse waves, Part 2: Hydrodynamic impact craters. Exp. Fluids 35 (6), 520–532.

Fritz, H.M., Hager, W.H., Minor, H.E., 2004. Near field characteristics of landslide generated impulse waves. J. Waterw. Port Coastal Ocean Eng. 130 (6), 287–302.

Heinrich, P., 1992. Nonlinear water waves generated by submarine and aerial landslides. J. Waterw. Port Coastal Ocean Eng. 118 (3), 249–266.

Heller, V., Hager, W.H., Minor, H.E., 2009. Landslide generated impulse waves in reservoirs: Basics and computation. ETH Zurich.

Heller, V., Hager, W.H., 2010. Impulse Product Parameter in Landslide Generated Impulse Waves. J. Waterw. Port Coastal Ocean Eng. 136 (3), 145.

Heller, V., Spinneken, J., 2013. Improved landslide-tsunami prediction: effects of block model parameters and slide model. J. Geophys. Res. Oceans 118 (3), 1489–1507.

Heller, V., Spinneken, J., 2015. On the effect of the water body geometry on landslide–tsunamis: physical insight from laboratory tests and 2D to 3D wave parameter transformation. Coast. Eng. 104, 113–134.

Heller, V., Bruggemann, M., Spinneken, J., Roger, B., 2016. Composite modelling of subaerial landslide–tsunamis in different water body geometries and novel insight into slide and wave kinematics. Coast. Eng. 109, 20–41.

Huang, B.L., Yin, Y.P., Wang, S.C., Tan, J.M., Chen, X.T., Liu, G.N., 2019. Analysis of Landslide Generated Impulse Waves. Science Press, Beijing (In Chinese).

Huang, Y., Hao, L., Xie, P., Xu, Q., 2009. Numerical simulation of large deformation of soil flow based on SPH method. Chin. J. Geotech. Eng. 31 (10), 1520–1524 (In Chinese).

Kamphuis, J.W., Bowering, R.J., 1970. Impulse waves generated by landslides. Proceedings of the 12th Coastal Engineering Conference ASCE 575-588.

Liu, G.R., Liu, M.B., 2003. Smoothed particle hydrodynamics: a meshfree particle method. World Scientific, Singapore.

Liu, P.L.F., Wu, T.R., Raichlen, F., Synolakis, C.E., Borrero, J.C., 2005. Runup and rundown generated by three-dimensional sliding masses. J. Fluid Mech. 536, 107–144.

Mcfall, B.C., Fritz, H.M., 2016. Physical modelling of tsunamis generated by three-dimensional deformable granular landslides on planar and conical island slopes. Proceedings of the Royal Society A: Mathematical, Physical and Engineering Science 472(2188): 20160052.

Meng, Z., 2018. Experimental study on impulse waves generated by a viscoplastic material at laboratory scale. Landslides 15 (6), 1173–1182.

Miller, G.S., Andy, Take, W.A., Mulligan, R.P., McDougall S., 2017. Tsunamis generated by long and thin granular landslides in a large flume. Journal of Geophysical Research: Oceans 122(1): 653-668.

Mohammed, F., Fritz, H.M., 2010. Experiments on tsunamis generated by 3D granular landslides, in: Mosher, D.C., Shipp, R.C., Moscardelli, L., Chaytor, J.D., Baxter, C.D. P., Lee, H.J., Urgeles, R. (Eds.), Submarine mass movements and their consequences. Springer, Dordrecht, pp. 705-718.

Mulligan, R.P., Take, W.A., 2017. On the transfer of momentum from a granular landslide to a water wave. Coast. Eng. 125, 16–22.

Monaghan, J.J., Kos, A., 2000. Scott Russell's wave generator. Phys. Fluids 12 (3), 622–630.

Monaghan, J.J., 2005. Smoothed particle hydrodynamics. Rep. Prog. Phys. 68 (8), 1703–1759.

Noda, E., 1970. Water waves generated by landslides. Journal of the Waterways, Harbors and Coastal Engineering Division 96(4): 835-855.

Panizzo, A., Bellotti, G., De, Girolamo, P., 2002. Application of wavelet transform analysis to landslide generated waves. Coastal Engineering 44(4): 321-338.

Panizzo, A., De, Girolamo, P., Petaccia, A., 2005 Forecasting impulse waves generated by subaerial landslides. Journal of Geophysical Research 110(C12).

Qiu, L., Jin, F., Lin, P., Liu, Y., Han, Y., 2017. Numerical simulation of submarine landslide tsunamis using particle based methods. J. Hydrodyn. 29 (4), 542–551.

Ren, K.J., Han, J.B., Lu, H., 2002. Experimental research on primary wave height generated by solid-type landslide. Yangtze River 43 (2), 43–45.

Rzadkiewicz, S.A., Mariotti, C., Heinrich, P., 1997. Numerical simulation of submarine landslides and their hydraulic effects. J. Waterw. Port Coastal Ocean Eng. 123 (4), 149–157.

Schwaiger, H.F., Higman, B., 2007. Lagrangian hydrocode simulations of the 1958 Lituya Bay tsunamigenic rockslide. Geochem. Geophys. Geosyst. 8 (7), Q7006.

Shi, C.Q., An, Y., Wu, Q., Liu, Q.Q., Cao, Z.X., 2016. Numerical simulation of landslide-generated waves using a soil–water coupling smoothed particle hydrodynamics model. Adv. Water Resour. 92, 130–141.

Shi, C.Q., 2018. Numerical Study on Generation Processes and Near-Field Characteristics of Landslide Induced Impulse Waves. University of Chinese Academy of Sciences, Beijing (In Chinese).

Vacondio, R., Mignosa, P., Pagani, S., 2013. 3D SPH numerical simulation of the wave generated by the Vajont rockslide. Adv. Water Resour. 59, 146–156.

Wang, W., Chen, G., Zhang, H., Zhou, S.H., Liu, S.G., Wu, Y.Q., Fan, F.S., 2016. Analysis of landslide-generated impulsive waves using a coupled DDA-SPH method. Eng. Anal. Boundary Elem. 64, 267–277.

Walder, J.S., Watts, P., Sorensen, O.E., et al., 2003. Tsunamis generated by subaerial mass flows. J. Geophys. Res. 108 (B5), 2236.

Watts, P., 1997. Water waves generated by underwater landslides. California Institute of Technology, Pasadena.

Watts, P., 2000. Tsunami features of solid block underwater landslides. Journal of waterway, port, coastal, and ocean engineering 126(3): 144-152.

Zhang, S.M., 2006. Handbook of Geological Engineering. China Architecture & Building Press, Beijing.

Zou, Z.Z., 2005. Water wave theories and their applications. Science press, Beijing.

Zweifel, A., Hager, W.H., Minor, H., 2006. Plane Impulse Waves in Reservoirs. Journal of Waterway, Port, Coastal, and Ocean Engineering 132(5): 358-368.

Zweifel, A., Zuccala, D., Gatti, D., 2007. Comparison between computed and experimentally generated impulse waves. J. Hydraul. Eng. 133 (2), 208–216.